Tectonophysics 679 (2016) 15–28

Contents lists available at ScienceDirect

Tectonophysics

journal homepage: www.elsevier.com/locate/tecto

Seismological evidence of an active footwall shortcut thrust in the Northern Itoigawa–Shizuoka Tectonic Line derived by the aftershock sequence of the 2014 M 6.7 Northern Nagano earthquake

Yannis Panayotopoulos *, Naoshi Hirata, Akinori Hashima, Takaya Iwasaki, Shin'ichi Sakai, Hiroshi Sato

Earthquake Research Institute, The University of Tokyo, 1-1-1 Yayoi, Bunkyo-ku, Tokyo 113-0032, Japan

ARTICLE INFO

Article history:
Received 10 July 2015
Received in revised form 8 April 2016
Accepted 10 April 2016
Available online 15 April 2016

Keywords:
Itoigawa–Shizuoka Tectonic Line
Active fault
Seismicity
Tectonic inversion
Double difference location
Japan

ABSTRACT

A destructive M 6.7 earthquake struck Northern Nagano prefecture on November 22, 2014. The main shock occurred on the Kamishiro fault segment of the northern Itoigawa–Shizuoka Tectonic Line (ISTL). We used data recorded at 41 stations of the local seismographic network in order to locate 2118 earthquakes that occurred between November 18 and November 30, 2014. To estimate hypocenters, we assigned low Vp models to stations within the Northern Fossa Magna (NFM) basin thus accounting for large lateral crustal heterogeneities across the Kamishiro fault. In order to further improve accuracy, the final hypocenter locations were recalculated inside a 3D velocity model using the double-difference method. We used the aftershock activity distribution and focal mechanism solutions of major events in order to estimate the source fault area of the main shock. Our analysis suggests that the shallow part of the source fault corresponds to the surface trace of the Kamishiro fault and dips 30°–45° SE, while the deeper part of the source fault corresponds to the downdip portion of the Otari–Nakayama fault, a high angle fault dipping 50°–65° SE that formed during the opening of the NFM basin in the Miocene. Along its surface trace the Otari–Nakayama fault has been inactive during the late Quaternary. We verified the validity of our model by calculating surface deformation using a simple homogeneous elastic half-space model and comparing it to observed surface deformation from satellite interferometry, assuming large coseismic slip in the areas of low seismicity and small coseismic slip in the areas of high seismicity. Shallowing of the source fault from 50°–65° to 30°–45° in the upper 4 km, in the areas where both surface fault traces are visible, is a result of footwall shortcut thrusting by the Kamishiro fault off the Otari–Nakayama fault.

1. Introduction

On November 22, 2014 a destructive earthquake with a local magnitude (M_{JMA}) of 6.7, struck Northern Nagano prefecture in Honshu, Japan. The earthquake, which we will refer to as the 2014 Northern Nagano Earthquake, occurred at local time 22:08:17 (UTC + 9) and its hypocenter was located by the Japan Metrological Agency (JMA) at a depth of 4.59 km (Fig. 1). Due to its proximity to the Itoigawa–Shizuoka Tectonic Line (ISTL) the main shock is inferred to have occurred on the Kamishiro fault segment of the Northern ISTL (Japan Meteorological Agency, 2014).

The ISTL is a prominent inland fault system which extends across Honshu Island from Itoigawa City on the Sea of Japan to Shizuoka City on the Pacific Ocean. It divides Honshu Island into NE and SW parts (e.g., Yabe, 1918)(Fig. 1). The ISTL is a key feature controlling the evolution of the Northern Fossa Magna (NFM) rift basin (Sato, 1994) since its creation in early Miocene. The NFM basin is part of a Miocene rift system that developed in the final stages of the opening of the Sea of Japan (25–15 Ma)(Otofuji et al., 1985; Yamaji, 1990). The area to the west of the NFM basin is occupied by pre-Neogene basement rocks, which consist of Mesozoic accretionary complex and granitic rocks and which are generally referred as the "inner zone" (Kano et al., 1990; Taira, 2001). The basin itself is filled mostly with more than 6-km-thick Miocene marine sediments (e.g. Kato, 1992; Takano, 2002) and displays significant folding on a NE-trending axis (Fig. 2). The stratigraphy of the basin is represented by a sequence of volcanic and volcanoclastic rocks, distal to proximal turbidities, and shallow marine to fluvial sediments (Kato, 1992, Takano, 2002). The basin has undergone shortening deformation since the Pliocene (3 Ma) (e.g. Sato, 1994) due to compressional inversion of a formerly extensional stress regime (e.g. Williams et al., 1989; Sato 1996).

The epicenter of the 2014 Northern Nagano Earthquake is located in the area between the surface traces of the Kamishiro and Otari–Nakayama faults (Kato et al. 1989, Nakata and Imaizumi, 2002; Kondo et al., 2008) (Fig. 1). The northernmost segment of the ISTL, the Kamishiro fault, represents the western boundary of the NFM basin and is considered to form a low-angle east-dipping thrust fault

* Corresponding author.
E-mail address: yannis@eri.u-tokyo.ac.jp (Y. Panayotopoulos).

http://dx.doi.org/10.1016/j.tecto.2016.04.019

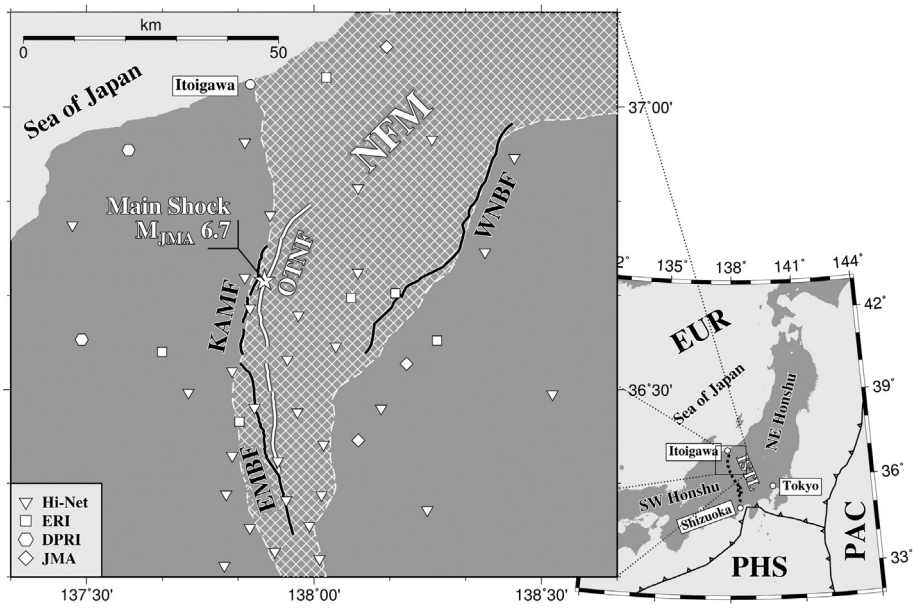

Fig. 1. Location map of the Kamishiro fault and Otari–Nakayama fault and distribution of stations of the permanent earthquake observation network in the area of study. Inverted triangles: stations of the High Sensitivity Seismograph Network of Japan (Hi-Net); Squares: stations operated by the Earthquake Research Institute of Tokyo University (ERI); Hexagons: stations operated by the Disaster Prevention Research Institute of Kyoto University (DPRI); Diamonds: stations operated by the Japanese Meteorological Agency (JMA). Cross-hatched area: approximate boundary of the Northern Fossa Magna Rift basin at 0 km depth mapped from surface geology (Geological Survey of Japan, 2003) and tomography studies (Panayotopoulos et al. 2014).White boxes indicate toponyms in the vicinity of the ISTL, Itoigawa: Itoigawa city; Shizuoka: Shizuoka city; Tokyo: Tokyo metropolitan area. PHS: Philippine Sea Plate; PAC: Pacific Plate; EUR: Eurasia Plate. White star: epicenter of the 2014 Northern Nagano Earthquake determined by JMA.

(Okumura et al., 1998; Sato et al., 2004). Its slip rate was estimated at ca. 1.5 to 5.4 mm/yr since the Late Pleistocene (Okumura et al., 1998; Matsuta et al., 2004), with a recurrence interval between 1258 and 1510 yr (Okumura, 2001). The slip sense of the portion of the ISTL south of the Kamishiro fault, nominally the East Matsumoto Basin fault, changes progressively from reverse to oblique strike-slip (Kondo et al., 2006; Kondo et al., 2008; Panayotopoulos et al., 2014). The strain accumulation rate along the Kamishiro and East Matsumoto Basin faults of the Northern ISTL, previous to the 2014 Northern Nagano Earthquake, has been determined from geodetic measurements (Sagiya et al., 2002; Sagiya et al., 2004). The GNSS(Global Navigation Satellite System) velocity data suggest a 10 mm/year horizontal displacement rate on a N110^{0}E direction (Sagiya et al., 2002). This indicates that the maximum horizontal principal strain axis in the central and northern ISTL is oblique to the strike of the ISTL and that the faults in the area have a significant left-lateral slip component (Sagiya et al., 2004). Focal mechanism solutions in the area suggest a complex stress regime of strike-slip and reverse faulting (Imanishi et al., 2010, Panayotopoulos et al., 2014).

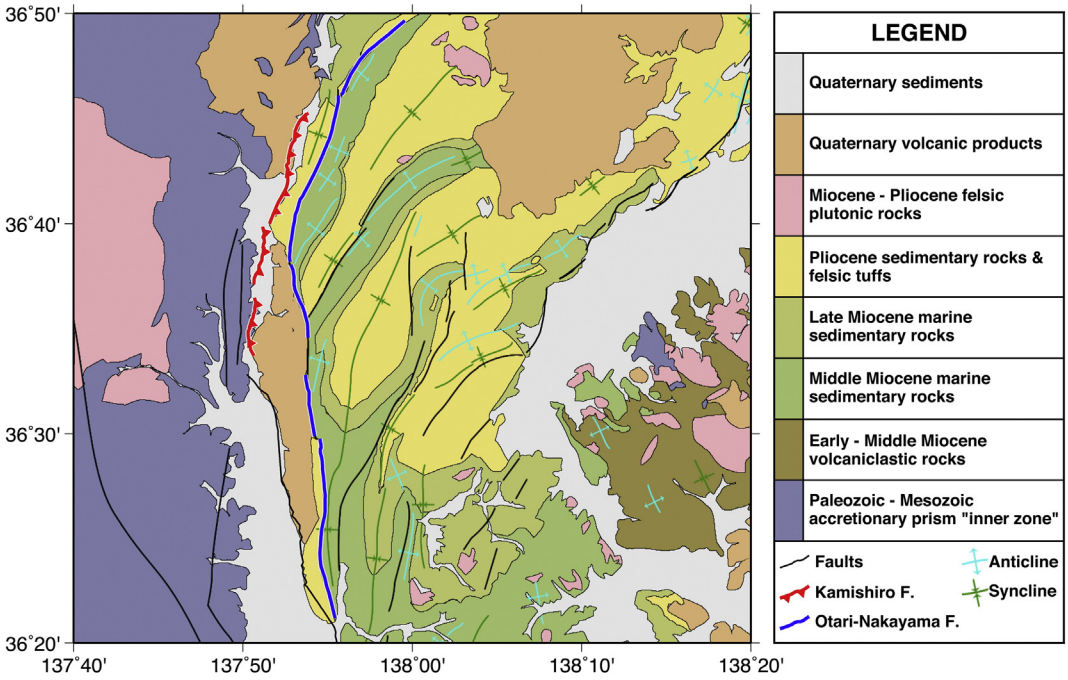

Fig. 2. Simplified geological map of the study area (after Editorial Committee of Civil Engineering Geologic Map of Kanto, 1996). Red line: surface trace of the Kamishiro fault. Blue line: surface trace of the Otari–Nakayama fault.

The surface trace and shallow geometry of the Kamishiro fault have been mapped in detail and it has been shown to be an active thrust fault (e.g., Sato et al., 2004; Takeda et al., 2004). On the other hand, the Otari–Nakayama fault, which runs parallel to the Kamishiro and East Matsumoto Basin faults, shows no geomorphological evidence of late Quaternary activity (Matsuta et al., 2004; Ueki, 2008). Some authors have suggested that it represents an earlier Quaternary surface trace of the ISTL which is no longer active (Ikeda, 1983; Sato and Hirata, 1998). Active fault slip has now shifted to the Kamishiro and East Matsumoto Basin faults located to the west of the previously active segment (Sato and Hirata, 1998). We cannot distinguish between in-sequence propagation of the thrust system (e.g. Boyer & Elliott, 1982) or footwall shortcut thrusting as an explanation for the shift in fault activity because, in the case of the Kamishiro and Otari–Nakayama faults, their geometry at depth is not well constrained. A footwall shortcut thrust is a characteristic feature of basins that are undergoing tectonic inversion. The geometry of the shortcut thrust is controlled by the geometry of extensional faults created during the opening of the basin (e.g. Williams et al., 1989). The reactivation of extensional faults that display high dip angles near the surface is mechanically difficult under the new compressional stress regime of the tectonic inversion. This leads to the formation of footwall shortcut faults that break off from the original high angle fault with a lower angle towards the surface (Powell, 1987).

The 2014 Northern Nagano earthquake and its well recorded aftershock sequence is a unique opportunity to understand the behavior of the active faults in Northern ISTL. In order to understand the mechanism responsible for the migration of active fault slip to its present location on the ISTL, we created a detailed map of the fault dimensions and configuration at depth. Our aim is to constrain the source fault geometry using seismological observations and to identify the links among present-day stress regime, coseismic surface deformation, and pre-existing tectonic structures, in order to understand how tectonic inversion is affecting present-day fault behavior and earthquake distribution on the western margin of the NFM basin.

2. Data and methods

The 2014 Northern Nagano earthquake occurred in an area covered by the permanent seismic networks operated by the JMA, the National Research Institute for Earth Science and Disaster Prevention (NIED), the University of Tokyo, and Kyoto University. For this study we obtained data from 41 seismic stations surrounding the Kamishiro fault, two of which are situated almost directly above the hypocenter of the 2014 Northern Nagano earthquake (Fig. 1). This enabled us to accurately locate the 2014 Northern Nagano earthquake and its aftershocks and to clarify their detailed temporo-spatial distribution. We compiled a dataset consisting of 1686 earthquakes reported in the JMA Unified Earthquake Catalogue (JMA-UEC) (Japan Meteorological Agency, 2014) that occurred between November 18 and November 30, 2014, and another 429 earthquakes, unique to this study, whose P- and S-phase arrivals we picked by visual observation. In total we used 32,273 P-phase and 22,314 S-phase arrivals from 2115 earthquakes, out of which we picked 25,631 P-phase and 12,877 S-phase arrivals while the rest are from JMA-UEC data.

Lateral heterogeneities in the area, reflecting the difference in crustal structure between the two sides of ISTL (Takeda et al., 2004; Panayotopoulos et al., 2014), create substantial error in accurately locating the hypocenters. To improve our estimation of the hypocenters, we followed a two-step process: we first estimated initial hypocenters using two one-dimensional (1-D) velocity models and station correction terms for travel-times that correspond to near surface local heterogeneity as in Panayotopoulos et al. (2014). Then we relocated them by the double difference method (DD) using relative travel times (e.g., Waldhauser and Ellsworth, 2000; Zhang and Thurber, 2003).

We used the maximum likelihood estimation algorithm, 'hypomh4', of Hirata and Matsu'ura (1987) and Sakai (2004) that allows us to assign a different 1-D P-wave velocity structure for each station. We constructed two 1-D P-wave velocity models from the three-dimensional (3-D) velocity structure in the Northern ISTL region given in Panayotopoulos et al. (2014). The respective S-wave velocity models are calculated by scaling the P-wave velocity models by a factor of 1.73, which is the average Vp/Vs ratio in the area (Panayotopoulos et al., 2014). We have allocated a low P-wave velocity model in the shallow parts of the crust for stations inside the NFM basin, while stations situated outside the basin have a velocity model close to that of the JMA all-Japan average (Fig.3).

The accuracy of hypocenter locations depends on random errors due to inaccurate picking and systematical errors induced by inadequate modeling of the velocity structure used in the determination. We were able to minimize random errors due to picking to as low as 0.03 s for the P and 0.05 s for the S phase by manually picking the phase arrivals. That makes the random error due to picking one order of magnitude smaller than the systematic errors due to inadequate modeling of the shallow velocity structure near the stations, typically on the order of one tenth of a second or higher. We corrected systematical errors due to velocity modeling by estimating station corrections for our dataset (Table 1). We first estimated initial hypocenters using the aforementioned velocity models without assuming station corrections. We then estimated the average travel time residuals for each station and solved iteratively in order to minimize the residual between the observed and calculated travel times (Sakai, 2004). We used the average residuals at each station estimated in one iteration as the station corrections for the next iteration. This process resulted in a root-mean-square (rms) residuals decrease from 0.182 s to 0.004 s for P-wave and 0.338 s to 0.005 s for S-wave with station corrections respectively (Table 1). After correcting for systematical errors, we are left with a remainder random-error that is the sum of picking errors and station correction estimation error distributions. We calculate an error covariance matrix for each earthquake and determine an average one standard error for our results of approximately 207 m for longitude (x direction), 156 m for latitude (y direction) and 414 m for depth (Fig. 4A-C).

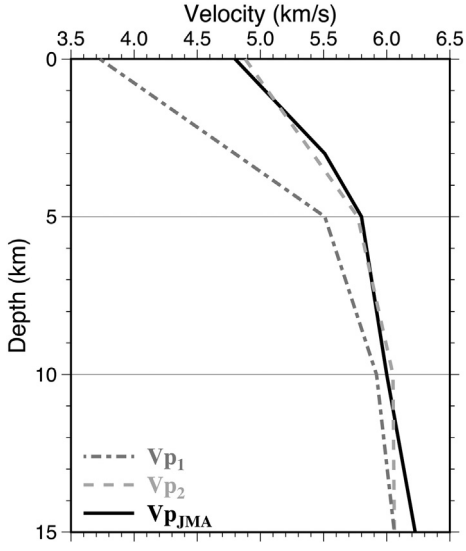

Fig. 3. P-wave velocity models used for hypocenter determination. Stations and grid points located inside the NFM basin were assigned low P-wave velocities for the shallow parts of the crust (Vp_1). For stations and grids outside that area, average crustal velocities (Vp_2) were derived from tomographic data (Panayotopoulos et al., 2014). The respective S-wave velocity models are calculated by scaling the P-wave velocity models by a factor of 1.73. The black solid line represents the 1-D P-wave velocity model adopted by the JMA (Vp_{JMA}) for hypocenter determination of the JMA Unified Earthquake Catalogue (JMA-UEC).

Table 1
Station location and station corrections. The columns are arranged from left to right with station name, latitude (deg), longitude (deg), elevation (m), number of P-phase arrivals used for the determination of station correction, P-phase arrival station correction (sec), standard deviation of the correction (sec), S-phase arrivals used for the determination of station correction, S-phase arrival station correction (sec), standard deviation of the correction (sec).

Station	Lat	Lon	Elv	Np	Δt_p	σ_{tp}	Ns	Δt_s	σ_{ts}
E.KYJ	36.56708	137.66610	1390	1151	0.185	0.169	817	0.566	0.227
E.TGA	36.66238	138.08161	760	1726	0	0.093	949	0.075	0.218
E.MTU	36.44265	137.83611	680	728	−0.099	0.110	478	0.004	0.229
E.HSJ	36.58710	138.27070	490	645	−0.121	0.108	448	−0.012	0.171
E.OMJ	36.67074	138.17888	506	573	−0.41	0.100	279	−0.831	0.312
E.NUJ2	37.05191	138.02683	210	432	0.321	0.099	406	0.975	0.190
N.OTNH	36.8089	137.9039	538	1778	−0.189	0.055	1694	−0.294	0.182
N.HKKH	36.6440	137.8594	698	593	−0.344	0.076	245	−0.764	0.255
N.OSTH	36.6317	137.9656	493	1980	−0.004	0.087	1966	0.069	0.186
N.OMYH	36.4680	137.8691	638	317	−0.507	0.120	62	−0.86	0.400
N.CHHH	36.4022	138.0208	623	326	−0.403	0.165	122	−0.299	0.407
NAKAMA	37.1060	138.1598	140	141	−0.13	0.125	23	0.065	0.641
NSAKAI	36.4098	138.0975	930	951	−0.17	0.147	823	−0.005	0.309
MATSUS	36.5458	138.2038	406	1400	−0.114	0.117	1139	−0.043	0.225
N.UOZH	36.7914	137.4689	52	905	0.009	0.126	276	0.242	0.284
N.NKNH	36.7434	138.3760	177	544	0.243	0.134	660	0.656	0.234
N.MSTH	36.2541	137.8591	417	619	−0.219	0.123	550	0.038	0.261
N.TKSH	36.2859	138.2491	504	555	−0.078	0.128	679	0.31	0.248
N.TUMH	36.4917	138.5244	888	150	−0.441	0.112	107	−0.375	0.312
N.MKOH	36.9425	138.2594	130	520	−0.271	0.092	102	−0.337	0.342
N.IGWH	36.9378	137.8480	49	1584	0.093	0.074	1582	0.382	0.159
N.MKGH	36.8569	138.0966	1153	1566	0.285	0.089	1028	0.581	0.197
N.ATYH	36.3036	137.9390	493	97	−0.195	0.140	25	−0.422	0.453
N.AAKH	36.3726	137.9203	483	236	−0.234	0.170	40	−0.344	0.512
N.MWDH	36.2118	137.9140	562	96	−0.534	0.122	27	−0.552	0.278
N.MAZH	36.1868	137.8030	760	73	−0.034	0.090	19	0.046	0.280
N.AHMH	36.3137	137.8072	982	221	−0.126	0.107	49	−0.089	0.205
N.MNYH	36.1987	138.0122	830	83	−0.238	0.123	8	−0.442	0.552
N.MANH	36.3127	138.0167	800	254	−0.366	0.139	96	−0.365	0.291
N.SNBH	36.5533	137.9415	705	1901	−0.18	0.099	1206	−0.45	0.250
N.HBAH	36.6984	137.8482	95	1958	−0.081	0.074	1954	−0.108	0.139
N.KMDH	36.4663	138.1474	290	580	−0.113	0.108	341	0.134	0.246
N.SSSH	36.5770	138.0479	401	1429	−0.35	0.090	759	−0.573	0.257
N.TGKH	36.7075	138.0964	813	1784	−0.167	0.080	1310	−0.309	0.207
N.NZWH	36.9102	138.4408	458	154	0.09	0.119	47	0.374	0.592
N.MMOH	36.2578	137.9898	539	172	−0.422	0.130	33	−0.417	0.508
N.IKSH	36.4598	137.9637	383	993	−0.235	0.109	495	−0.425	0.325
N.OM2H	36.5327	137.8201	718	1290	−0.041	0.124	913	0.046	0.269
N.HOTH	36.3824	137.8201	613	197	−0.089	0.094	145	0.067	0.196
DP.AHJ	36.92389	137.59229	230	929	0.029	0.105	220	0.26	0.311
DP.TYJ	36.58887	137.48915	785	289	0.266	0.114	100	0.702	0.264

In the next step we relocated the hypocenters with the 3-D velocity model obtained by Panayotopoulos et al. (2014) using the 'tomoDD' algorithm (Zhang and Thurber, 2003). We fixed the 3-D velocity structure and estimated hypocenter locations without modification of the velocity model, because in the present study station coverage does not allow us to resolve a detailed 3-D velocity distribution inside the aftershock area. Thus, we focused on a hypocenter distribution determined by relative travel times. Since the aftershock sequence is spread in an area of a few tens of kilometers, we allowed events to be linked as neighbors with a maximum separation distance of 1.5 km. This condition resulted in 12,443 linked event pairs with an average separation of 0.53 km that produced 115,872 P-phase and 73,185 S-phase relative travel times.

We applied the station corrections obtained in the previous step (Table 1) and ran the 'tomoDD' algorithm iteratively 17 times. The introduction of station corrections is effective for locations constrained by an absolute travel time. We then proceeded relocating the hypocenters iteratively following the weighting scheme described below. We started the ratio of absolute to relative time with 1:0.5 for the first 3 iterations and progressively weighted the relative times higher, 1:1, in the next 6 iterations, 0.5:1 in the next 4 iterations and 0.1:1 in the last 4 iterations. This process resulted in a 72% reduction of the weighted rms residuals from 0.216 s to 0.061 s. The average one standard error for the DD relocations is approximately 155 m for longitude (x direction), 144 m for latitude (y direction) and 226 m for depth (Fig. 4D-E).

In addition, we estimated focal mechanism solutions for our relocated hypocenters for the first major foreshock, the main shock, and most of the major aftershocks (Table 2). We manually picked polarities of P-arrivals for the network stations in wider central Japan and determined focal mechanisms by the HASH algorithm (Hardebeck and Shearer, 2002; Hardebeck and Shearer, 2003). We only estimated the mechanisms of earthquakes for which we were able to pick a clear phase arrival in more than 50 stations. We conducted a grid search in order to estimate the strike, dip, and rake angle of the best fit solution and followed the same focal mechanism solution quality classification procedure as in Hardebeck and Shearer (2002). The focal mechanism solutions are classified with decreasing quality from A to F depending on (1) the average misfit of the first-motion polarities, (2) the rms uncertainty between the set of acceptable mechanisms and of the preferred fault plane mechanism, (3) the station distribution ratio, (4) the probability of mechanisms within 45^0 of the preferred fault plane mechanism, (5) maximum gaps in the incidence, and (6) take-off angles and total number of polarities used. Only well determined focal mechanisms of quality A and B are taken into consideration when we interpret our results with average misfit in polarities <0.2, rms fault plane uncertainties <25°, station distribution ratios >0.5 and mechanism probability >0.85.

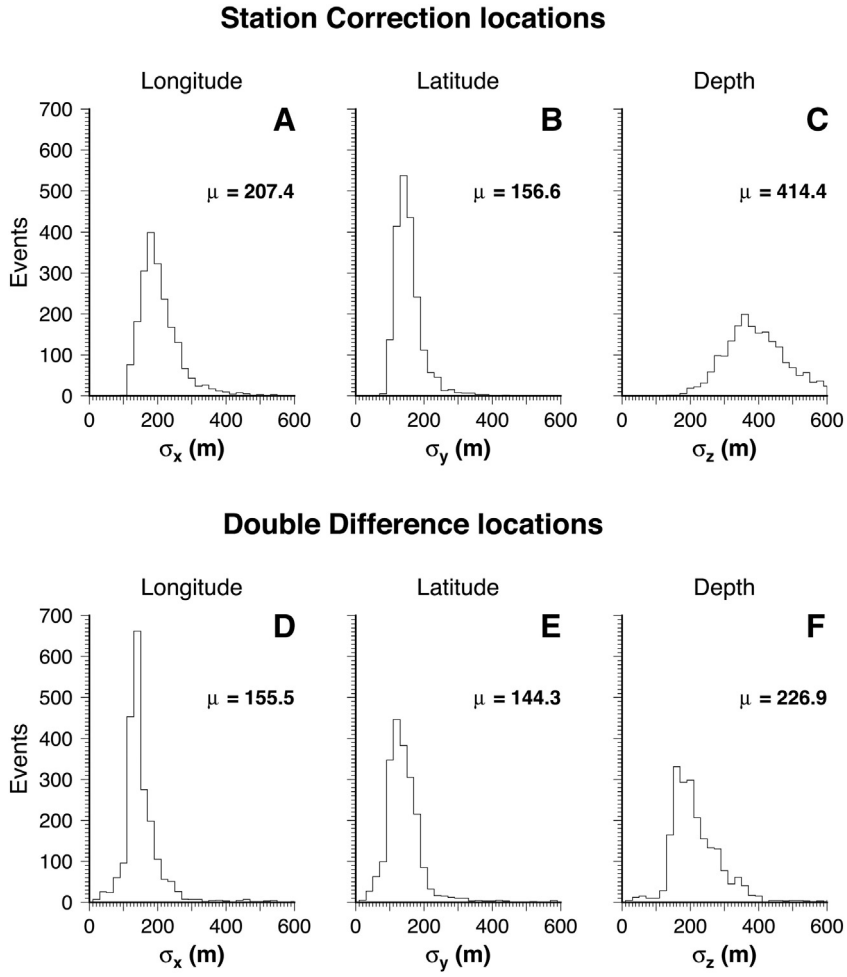

Fig. 4. Distribution of random errors for hypocenter locations. A–C) one standard error distributions estimated by the sum of picking errors and station correction estimation errors. D–E) one standard error for double-difference hypocenter locations.

Table 2
Hypocenter location and focal mechanism solutions determined by first motion polarity arrivals for the first major foreshock, the main shock, and major aftershocks. F-Strike, F-Dip and F-Rake denote the CMT solutions estimated by NIED using F-net for the same events (National Research Institute for Earth Science and Disaster Prevention, 2014).

Event #	Origin time		M_{jma}	Longtitude	Latitude	Depth (km)	Strike	Dip	Rake	Quality	F-Strike	F-Dip	F-Rake
1	2014/11/18	18:29:31.96	2.8	137.913525	36.690580	3.202	233	44	128	A			
2	2014/11/22	22:08:17.46	6.7	137.913232	36.687032	3.534	257	45	162	A	241	47	117
3	2014/11/22	22:13:47.28	3.5	137.948112	36.770085	5.279	235	66	117	A			
4	2014/11/22	22:15:39.56	3.3	137.915202	36.678593	3.716	232	62	107	A			
5	2014/11/22	22:37:48.86	4.5	137.932080	36.768197	2.967	225	62	132	B			
6	2014/11/22	22:54:59.48	3.8	137.916813	36.734546	2.852	19	43	77	A			
7	2014/11/22	23:26:02.68	3.2	137.965837	36.762341	7.369	231	42	129	A			
8	2014/11/22	23:56:50.32	2.2	137.885140	36.631226	2.391	230	73	109	A			
9	2014/11/23	00:23:28.11	3.0	137.907308	36.606999	4.865	230	60	119	B			
10	2014/11/23	02:31:00.31	2.5	137.902295	36.652747	4.570	222	55	121	B			
11	2014/11/23	04:52:24.41	3.2	137.883838	36.616016	3.412	307	27	−39	B			
12	2014/11/23	05:33:24.21	3.7	137.929997	36.748682	4.689	220	83	−173	B	219	36	180
13	2014/11/23	07:16:47.34	3.3	137.913070	36.739596	2.576	215	41	109	B			
14	2014/11/23	12:15:19.36	3.0	137.906641	36.735262	5.649	238	62	156	A			
15	2014/11/23	12:46:36.47	4.4	137.903499	36.732918	5.922	219	79	−169	A	224	45	172
16	2014/11/23	15:27:49.60	3.0	137.908561	36.733167	5.205	216	88	−126	A			
17	2014/11/23	15:56:44.09	3.4	137.906527	36.733049	4.957	221	82	−171	B			
18	2014/11/24	06:12:19.08	3.6	137.928988	36.774825	4.428	213	86	171	A	219	52	170
19	2014/11/24	18:34:59.20	2.9	137.917708	36.653992	6.610	243	49	144	A			
20	2014/11/25	06:26:55.16	3.9	137.921484	36.753931	4.123	222	82	−165	A	223	44	178
21	2014/11/28	13:13:21.15	3.6	137.907699	36.730168	4.327	215	77	−174	B	220	64	162
22	2014/11/29	02:38:10.55	3.1	137.906624	36.729097	4.049	218	78	−163	A			

3. Results

We have plotted the relocated hypocenters from November 18 to November 30, 2014 in the vicinity of the Northern ISTL and compared it to those published in the JMA-UEC (Fig. 5). Well-determined focal mechanisms are also shown in Fig. 5. Most of the hypocenters are distributed in the area to the east of the surface trace of the Kamishiro fault, inside and below the Miocene sediments filling the NFM basin. Our relocations appear to be shifted 2–3 km towards the east and also 3–4 km shallower than the locations reported in the JMA-UEC (Japan Meteorological Agency, 2014). The main shock is located at 36.687032° N, 137.913232° E, 3.534 km deep, which is approximately 2.2 km east and 1 km shallower than that listed in JMA-UEC (Table 2). The differences are statistically significant according to our error analysis mentioned before. This is due to the fact that in the velocity models and station corrections we used for the hypocenter location we considered low velocities inside the NFM basin and local lateral heterogeneities, while the JMA uses the average 1-D velocity model for all-Japan without station corrections (Fig. 3, Table 1).

The aftershocks are distributed for approximately 27 km along the Kamishiro fault trace and range from the surface to approximately 10 km depth. Considering variations in the apparent density and number of aftershocks, we have split the area along the Kamishiro fault into 5 segments of roughly equal dimension (I to V), each 14 km long

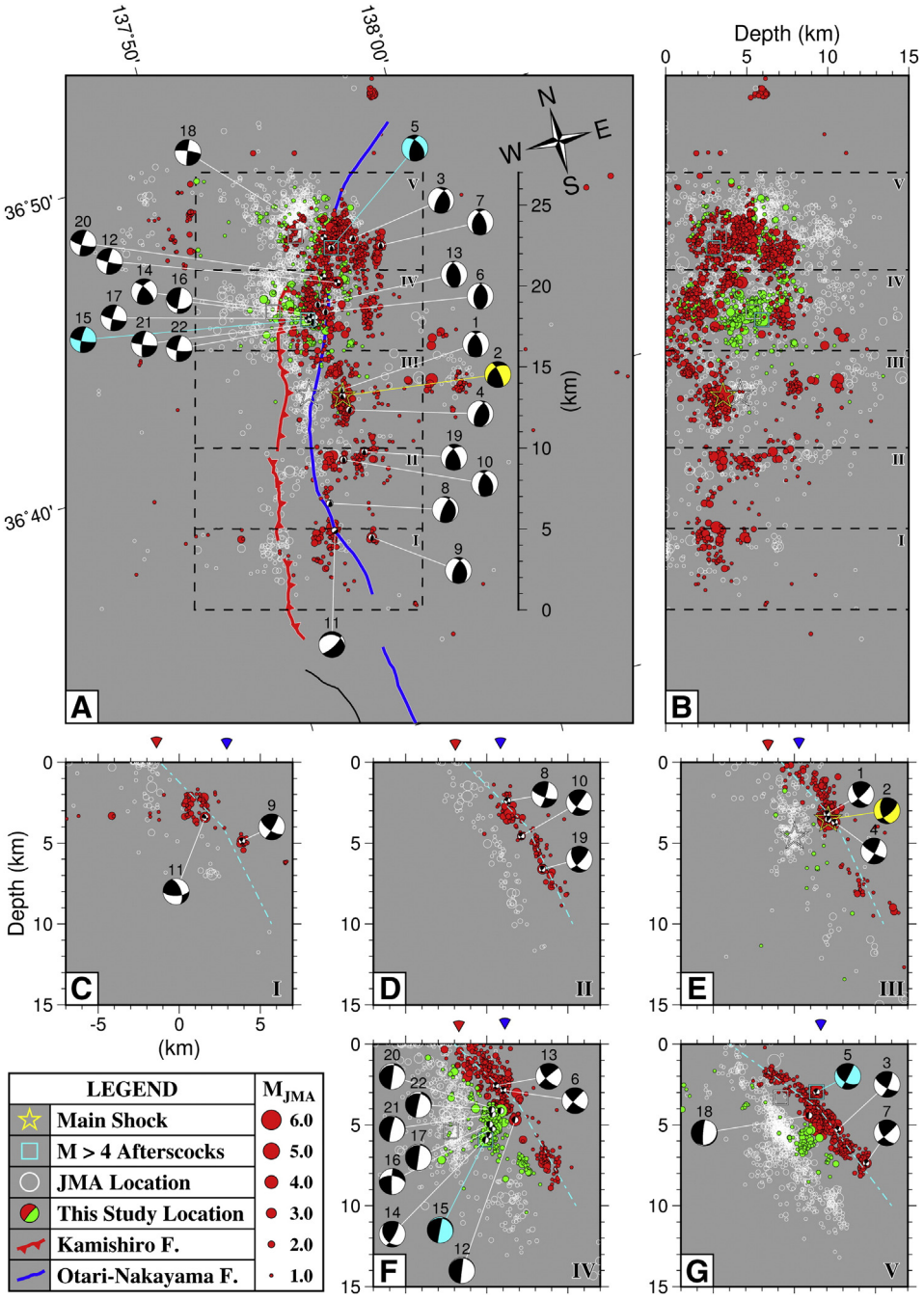

Fig. 5. JMA-UEC hypocenter locations and double-difference (DD) relocated hypocenter locations. A) Plot of JMA-UEC epicenters (white rings) and DD relocated epicenters (red circles). Yellow focal mechanism: main shock (earthquake 2,), Cyan focal mechanism: M > 4 aftershocks. Focal mechanisms are plotted showing the lower hemisphere. B) Hypocenter distribution with depth along the Kamishiro fault from south to north. C–G) Cross-sections across the Kamishiro fault from south to north. Each plot shows aftershocks occurring within the indicated segments, I–V. Yellow focal mechanism: main shock (earthquake 2), Cyan focal mechanism: M > 4 aftershocks. Focal mechanisms are plotted showing the back hemisphere. Red-colored aftershocks belonging to group (1) lie within ±1 km of the cyan dashed line. Green-colored aftershocks belonging to group (2) lie farther than ±1 km from this line.

and 5 to 6 km wide, which extend from the surface to a depth of 15 km (Fig. 5C–G). The aftershock distribution is not homogenous along strike or with depth. Along strike, it appears to be dense in segments IV and V, and sparse in segments I, II, and III where the main shock hypocenter is located. Within segment II there is a clear trend with depth of the hypocenter distribution that changes from a shallow to a steeper angle at approximately 4 km depth (Fig. 5D). Between 4 and 9 km depth, the hypocenters follow a linear trend on a plane that dips approximately 60^0 ~ 65^0 towards the southeast while above 4 km, the dip changes to 40°–45°. If we project the 40–45° dipping plane from 4 km depth to the surface, the resulting trace coincides with the surface mapped fault trace of the Kamishiro fault. Likewise, if we project the 60°–65° dipping plane from 9 km to the surface, the resulting trace coincides with the mapped fault trace of the Otari–Nakayama fault. There is no similarly obvious clustering in the deeper sections of neighboring segment I (Fig. 5C). The seismicity in segment I is largely shallow, occurring mostly above 5 km depth. The seismicity has a similar linear trend on the segment III plane as on the segment II plane, starting at a depth of approximately 3.5 km with a dip of 40°–45° that extends almost to the surface fault trace of the Kamishiro fault (Fig. 5E). In segment IV, there is a high volume of aftershocks, which are distributed throughout but the pattern of distribution is less clear. There is a weak clustering of hypocenters inside this segment following a similar change from a shallow to a steeper angle at approximately 4 km depth (Fig. 5F). Segment V displays a similar trend in the hypocenter distribution as in segment II, but at shallower angles: The 0–4 km depth plane dips 30^0 ~ 35^0 towards the southeast while the 4–9 km depth plane dips 50°–55° (Fig. 5G). In addition, inside segments IV and V a prominently expressed near-vertical clustering of earthquakes is visible, starting from the point where the 2 planes come together at approximately 4 km depth and extending to 8 km depth inside the footwall area of the fault (Fig. 5F,G).

The focal mechanism of the main shock describes a WNW–ESE reverse fault with a strike-slip component (Fig. 5, earthquake 2). Focal mechanism solutions are divided into two groups. Group (1) includes the foreshock (Fig. 5, earthquake 1), the main shock (Fig. 5, earthquake 2), and the first major aftershock (Fig. 5, earthquake 5). This group shows reverse-oblique slip with a WNW–ESE compressional axis. Group (2) includes the second major aftershock (Fig. 5, earthquake 15) and shows strike-slip movement with an WNW–ESE compressional axis and NNE–SSW extensional axis. Aftershocks in group (1), with the reverse-oblique behavior, are distributed on or near the east-dipping distribution (Fig. 5, earthquakes 3, 4, 6, 7, 8, 9, 10, 13 and 19). Aftershocks in group (2) with strike-slip behavior occur mainly off the main cluster on the west-dipping cluster inside the footwall area of the fault (Fig. 5, earthquakes 12, 14, 15, 16, 17, 18, 20, 21 and 22). A distinct foreshock sequence began on November 18, 2014, 4 days before the main shock; it was confined to a 1 × 1 × 1 km volume within segment III at a depth of approximately 3 km, close to the hypocenter of the main shock (Fig. 6A,C). The largest foreshock had a focal mechanism similar to that of the main shock. (Fig. 6A,B, earthquakes 1 and 2 respectively). The aftershock sequence for the 24 h following the main shock is shown in Fig. 6B. The aftershocks from the first 1.5 h occur in an area of 17 km × 10 km in segments II–V and slowly expand to segment I over the next 22.5 h (Fig. 6D). In addition, there is significantly more activity in segments IV and V than in the other three segments of the fault. In segment V, the first major M_{JMA} 4.5 aftershock (Fig. 6B, earthquake 5) occurred at 22:37:47 (UTC + 9) approximately 30 min after the main shock. It was followed by another M_{JMA} 4.4 aftershock (Fig. 6B, earthquake 15) that occurred in segment IV on November 23, 12:46:36 (UTC + 9). This activity did not diminish with time but rather continued in segments IV and V for the duration of our study interval. We observed that major aftershocks with reverse fault mechanisms are restricted to the first few hours after the main shock (Fig. 6B, earthquake numbers 3, 4, 5, 6, 7, 8, 9 and 10). On the other hand, major aftershocks with a predominantly strike-slip mechanism start several hours after the main shock and occur repeatedly throughout November 2014 (Fig. 6A, B).

4. Discussion

4.1. Source fault geometry

The aftershock distribution is well constrained by the present study. Relocated aftershocks have location errors of less than a few hundred meters, accurate enough to correlate with geologically mapped faults at surface. In addition, our relocated hypocenters are shifted several km away from the JMA reported locations which means that our estimation accuracy is one order of magnitude smaller than the total shift in the final position. The finely clustered earthquakes in segments II, III and V are distributed close enough to the source fault of the Northern Nagano earthquake to help us delineate its surface. In order to better understand the aftershock distribution pattern, we color-coded the aftershock distribution trends relative to the faults at depth, assuming the Kamishiro fault is a low-angle thrust fault (Okumura et al., 1998; Sato et al., 2004) and the Otari–Nakayama fault is a high-angle fault (Kato, 1992; Matsuta et al., 2004; Ueki, 2008). Following Felzer and Brodsky (2006) who showed that aftershocks are distributed close to but not exactly on the fault plane, we assume that events which lie within ± 1 km of the fault plane are aftershocks that were directly triggered by the main shock. We display aftershocks that lie within ± 1 km of either the low angle 30°–45° SE-dipping plane or the high angle 50°–65° SE-dipping plane marked by the cyan dashed line in Fig. 5C–G in red color. Green-colored aftershocks lie farther than ± 1 km from these planes. The red-colored clusters contain events with reverse-oblique type focal mechanisms (group 1), while the green-colored clusters contain mainly events with strike-slip type mechanisms (group 2). In addition, most major aftershocks with a reverse-oblique mechanism occurred in the first few hours of the aftershock sequence (Fig. 6, earthquakes 3 to 10). We consider the area defined by the red-colored clusters, containing oblique-thrust mechanisms, to represent the source fault (Fig. 5C–G). Thus we propose a source fault geometry model suggesting that the Kamishiro fault corresponds to the shallower part of the fault while the Otari–Nakayama fault to its deeper part.

We have split the source fault into 10 planar faults, in order to distinguish between the shallower and deeper parts of the source fault (Table 3). The shallow part (a) of the source fault from the surface to approximately 4 km depth dips with an angle of 30°–45° SE and the deeper part of the source fault (b) from 4 km to 10 km depth dips with an angle of 50°–65° SE (Fig. 7A). The steepening of fault dip appears to occur at the inferred bottom of the NFM basin (Panayotopoulos et al., 2014). Hence, the source fault dips more steeply in the pre-Neogene basement than in the Miocene sedimentary strata of the basin itself (Fig. 7B). Previous studies suggest that the Kamishiro fault forms a low-angle ~20° thrust fault (Okumura et al., 1998; Sato et al., 2004). We find that this is likely to be true only for the part of the source fault above 4 km depth in the NFM basin, based on the distribution of aftershocks after relocation, although the dip angle determined by our data is slightly steeper. In contrast, if we project the deeper, more steeply-dipping part of the source fault to the surface we find that it coincides with the surface fault trace of the Otari–Nakayama fault.

4.2. Fault segmentation

Our results suggest that the shallow parts of the source fault in the NFM basin with dips of 30°–45° are favorably oriented for a thrust fault mechanism. The same cannot be said for the part of the source fault below the NFM at depths greater than 4 km. The steeper dip angles of 50°–65° make it unfavorably oriented for a pure thrust mechanism. Recent studies suggest that the slip sense of the ISTL changes in the areas south of the Kamishiro fault from thrust to reverse-oblique slip (Kondo et al., 2006; Kondo et al., 2008; Panayotopoulos et al., 2014). The dip angle of the deeper part of the source fault resembles the dip angle in the central ISTL (Kondo et al., 2008; Panayotopoulos et al., 2014). It is plausible that some portion of strike-slip movement may

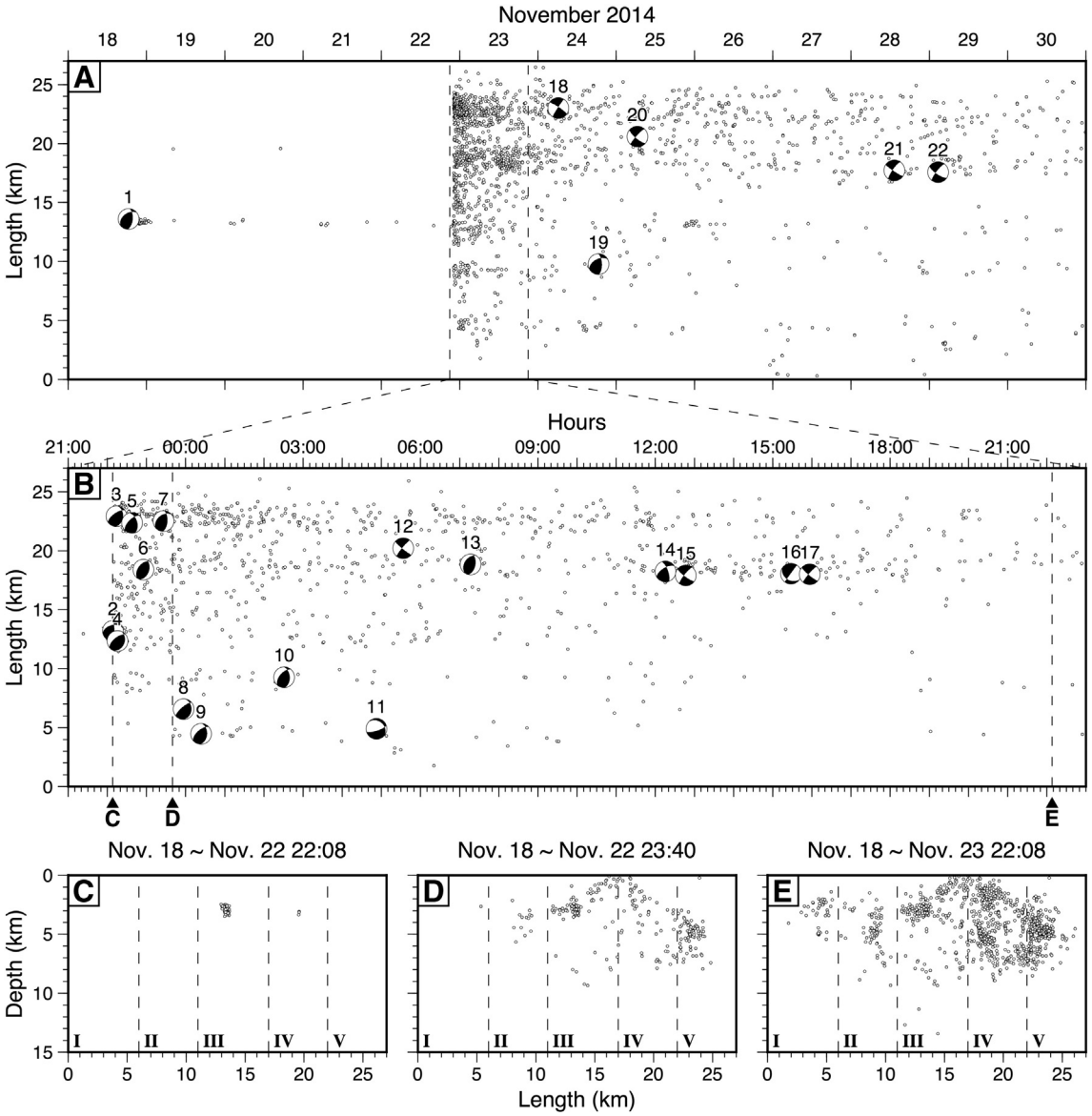

Fig. 6. Temporo-spatial distribution of seismicity. A) Seismic activity along the Kamishiro fault from 18 to 30 November 2014. B) Detailed view of seismic activity during the first 24 h after the main event. C) Cumulative plot of foreshock activity on a cross section along the fault from November 18, 00:00 to November 22, 22:08. D) Cumulative plot of foreshock and aftershock activity from November 18, 00:00 to November 22, 23:40. E) Cumulative plot of foreshock and aftershock activity from November 18, 00:00 to November 23, 22:08. Focal mechanisms are plotted showing the lower hemisphere.

be preserved at the deeper parts of the ISTL in its more northerly reaches. Indeed, the focal mechanism solution of the main shock is not pure reverse but rather reverse-oblique (Fig. 5, earthquake 2). Our estimated first motion solution of the main shock, similar to the first motion solution estimated by JMA (Japan Meteorological Agency, 2014), displays a strong strike-slip component. The centroid moment tensor (CMT) solution estimated by NIED using the Full Range Seismograph Network of Japan stations (F-Net) (National Research Institute for Earth Science and Disaster Prevention, 2014), displays a strongly reverse type mechanism (Table. 2). These observations do not contradict our findings, since the initiation of the rupture could have started in the deeper parts of the fault with a strong lateral movement and changed to a thrust mechanism as it propagated to the shallower parts.

The focal mechanism solutions for aftershocks, in red, on the deeper section of the proposed source fault are different from the focal mechanism solutions for aftershocks, in green, located off the source fault. Aftershock mechanisms on the proposed source fault of the Northern Nagano earthquake show largely reverse motion with a strike-slip component which reflects both the present stress field and inherited fault geometry. On the other hand, we observe that the strike-slip component is dominant off the source fault in the footwall block, where a branch fault with a steeper dip angle of 80° is located (Fig. 5F,G). Our estimated first motion solutions for these events display a strike-slip mechanism comparable to the CMT solutions done by NIED (National Research Institute for Earth Science and Disaster Prevention, 2014), (Table. 2). These aftershocks occurred several hours after the main shock, suggesting that they represent a delayed rupture triggered off-fault by the Northern Nagano main shock. This branch fault may have been created during the rifting process of the NFM in a tensional stress field and reactivated by the present day compressional (inverted) tectonic regime.

4.3. Aftershocks and coseismic slip

The relocated aftershocks are concentrated in several distinct clusters along the Kamishiro fault. In general, the shallower extension of

Table 3
Coordinates of the proposed source fault model (km) and major slip area. The center of the coordinate system is located at the JMA epicenter of the Northern Nagano Earthquake on lat. 36.69, lon. 137.89 at mean sea level. The system follows a left hand rule with the z axis positive downwards and is rotated 15° clockwise from the north (y axis).

	I			II			III			IV			V		
	x	y	z	x	y	z	x	y	z	x	y	z	x	y	z
Fault model															
a	−1.2	−13	0	−1.4	−8	0	−1.4	−3	0	−0.8	3	0	−2.2	8	0
	−1.4	−8	0	−1.4	−3	0	−0.8	3	0	−2.2	8	0	−4	14	0
	2.5	−8	4	2.5	−3	4	2.5	3	3.6	2	8	3.8	1.5	14	4
	2.7	−13	4	2.5	−8	4	2.5	−3	4	2.5	3	3.6	2	8	3.8
b	2.7	−13	4	2.5	−8	4	2.5	−3	4	2.5	3	3.6	2	8	3.8
	2.5	−8	4	2.5	−3	4	2.5	3	3.6	2	8	3.8	1.5	14	4
	5.3	−8	10	5.3	−3	10	5.5	3	10	5.75	8	10	6	14	10
	5.7	−13	10	5.3	−8	10	5.3	−3	10	5.5	3	10	5.75	8	10
Major slip area															
a				−0.42	−8	1	−1.4	−3	0						
				−1.4	−3	0	−0.8	3	0						
				1.52	−3	3	2.5	3	3.6						
				0.55	−8	2	2.5	−3	4	2.5	3	3.6			
b							2.5	−3	4	2.5	3	3.8			
							2.5	3	3.6	2	8	3.8			
							5.5	3	10	2.85	8	5.3			
							5.3	−3	10	4.56	3	8			

the aftershock distribution above 4 km depth coincides with the surface trace of the Kamishiro fault, clearly shown in the cross-sections of segments I, II, III, IV (Fig. 5C–F). The InSAR data analyzed by the Geospatial Information Authority of Japan (GSI) suggest a maximum 1 m of uplift and a maximum 20 cm of subsidence to the east and to the west of the Kamishiro fault trace respectively (Geospatial Information Authority of Japan, 2014). In addition, geomorphological surveys after the 2014 Northern Nagano earthquake show intermittently continuous surface raptures along the mapped Kamishiro fault trace and no surface rupture along the Otari–Nakayama fault trace (Geological Survey of Japan, AIST, 2014). The maximum deformation coincides with segment III where the main shock was located and where aftershock activity was low (Fig. 7A,C). Conversely, surface deformation progressively diminishes in segments IV and V where aftershock activity is high.

Previous studies have linked the spatial distribution of aftershocks to the coseismic slip distribution. The 1984 Morgan Hill earthquake (M_w 6.1) (e.g: Mendoza and Hartzell, 1988; Oppenheimer et al., 1990), the 1989 Loma Prieta earthquake (M_w 6.9) (e.g: Beroza and Zoback, 1993) and the 1995 Hyogo-ken Nanbu earthquake (M_{JMA} 7.2) (e.g: Hirata et al., 1996) showed few aftershocks in the area where the largest coseismic slip occurred and many aftershocks in the small slip areas surrounding the main shock area. A similar pattern of low aftershock seismicity close to the main shock has been observed after other major earthquakes in Japan, like the 1995 Hyogo-Ken Nanbu earthquake (Hirata et al., 1996), 2004 Mid-Niigata Prefecture Earthquake (Kato et.al., 2010) and the offshore Pacific coast Tohoku Earthquake in 2011 (Asano et.al., 2011; Shinohara et al., 2012). More recent statistical analyses of the aftershock distributions of the 1992 Landers earthquake (M_w 7.3), the 2000 Tottori earthquake (M_w 6.6), the 2004 Parkfield earthquake (M_w 5.9) (Woessner et al., 2006) and the 2004 Mid-Niigata Prefecture earthquake (M_{JMA} 6.6) (Kato et al., 2010) show a strong correlation between small coseismic slip and high concentration of aftershocks, suggesting that this activity was triggered by increased shear stress due to the main shock slip. The authors of the aforementioned studies attribute the absence of aftershocks in the area of largest coseismic slip to total stress release or a weak fault interface which cannot sustain further deformation.

The relocated aftershock sequence of the 2014 Northern Nagano earthquake follows the aftershock patterns of other major earthquakes. We can clearly distinguish between areas of low seismicity inside segments II, III, and IV and areas of high seismicity inside segments IV and V (Fig. 7A). The areas of low seismicity form a contiguous region which appears as a prominent seismic gap between the red-colored clusters of aftershock activity on the proposed source fault surface. We represent this region with a cyan color cross-hatched surface (Fig. 7A). When compared to surface displacement along the surface fault trace in the InSAR data (Fig. 7C), our analysis suggests that inside segments IIa and IIIa from 0 to 4 km depth and segments IIIb and IVb from 4 to 10 km depth experienced the largest coseismic slip, as opposed to segments Ia, IVa and Va from 0 to 4 km depth and segments Ib, IIb and Vb from 4 to 10 km depth where we assume small coseismic slip. This is expressed by the short-wavelength, high-deformation area between the surface fault traces of the Kamishiro and Otari–Nakayama faults in segments II and III, and the long-wavelength, low-deformation area to the east of the Otari–Nakayama fault trace in segments II, IV and IV (Fig. 7C). We have divided our fault model so that segment I is the southernmost area where we observed aftershocks. Segment IIa is the southernmost area where we assumed major coseismic at the shallow parts of the source fault. Segment III, the main shock area, is the northernmost area we assumed major coseismic slip in the shallow parts of the fault at segment IIIa, and the southernmost area we assumed major coseismic slip on the deeper parts of the source fault at segment IIIb. Segment IVb represents the northernmost area we assumed major coseismic slip on the deeper parts of the source fault. Finally, segment V is the northernmost area we observed aftershocks.

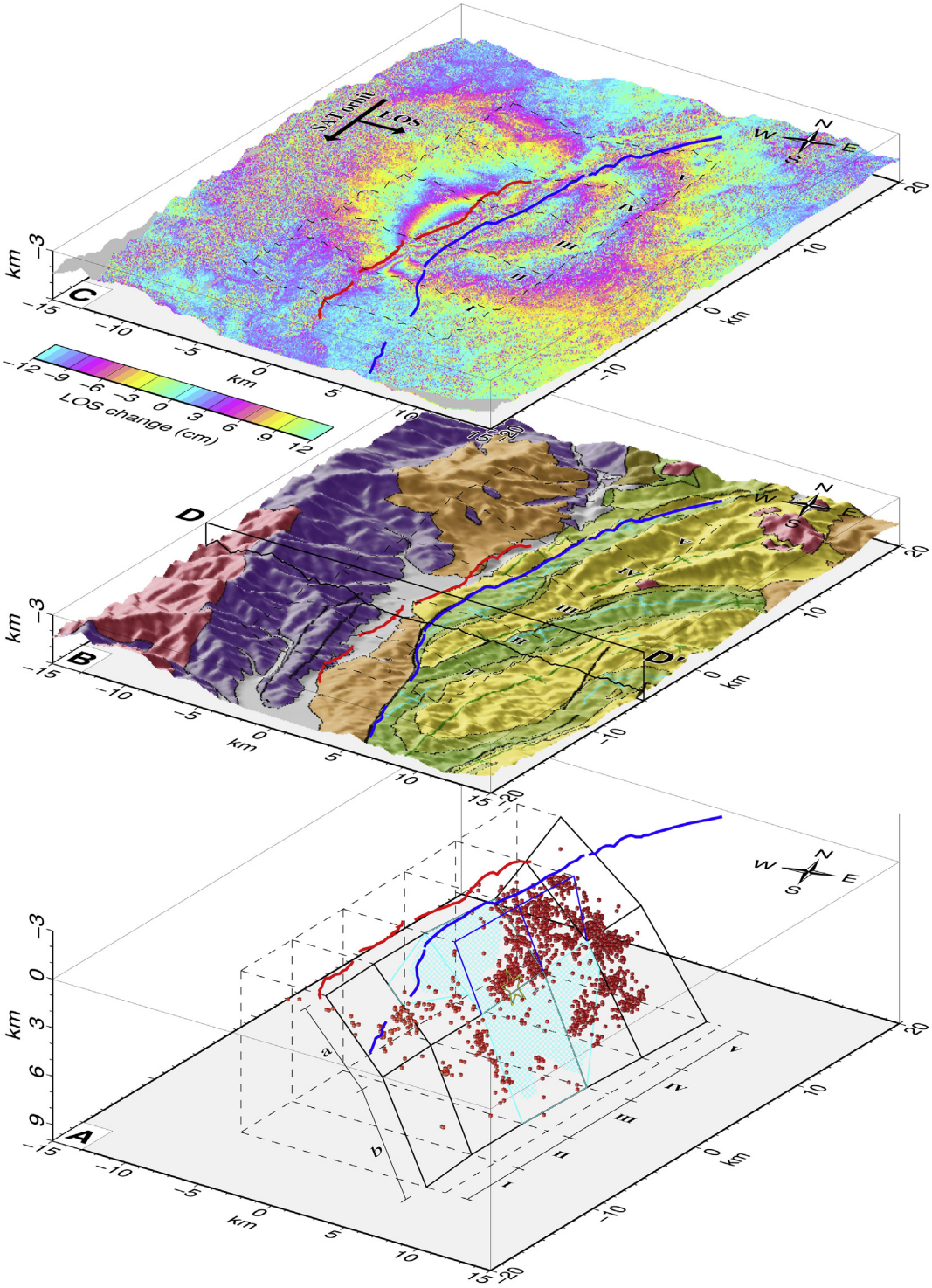

Fig. 7. Correlation of the fault model with observed crustal deformation and surface geology–topography. Red line: surface trace of the Kamishiro fault. Blue line: surface trace of the Otari–Nakayama fault A) 3-D fault model derived by the clustering the DD relocated hypocenters. Only aftershocks that are within ±1 km of the estimated source fault model are plotted. The cyan cross-hatched area represents major seismicity gaps. Yellow star: Main shock. Black polygons: source fault. Cyan polygons: major slip areas. Blue polygons: shallow parts of the Otari–Nakayama fault (0–4 km) B) 3-D map of the surface geology and topography along Kamishiro fault. See Fig. 2 for geological map legend. The surface expression of the northern end of the source fault fault in segments IV and V has probably been covered by Quaternary volcanism. C) InSAR plot analyzed by GSI from ALOS raw data of JAXA, METI superimposed on a topographical relief map (Geospatial Information Authority of Japan, 2014). Satellite data suggests a maximum 1 m of uplift to the east of the fault trace and a maximum 20 cm of subsidence to the west of the fault trace in segment III.

The previously-mapped Kamishiro active fault trace ends in segment IV, where pre-Neogene basement rocks that constitute the footwall of the fault have been covered by andesitic lavas and volcaniclastics in the Pleistocene (Nakano et al., 2002). Our results suggest that the shallow part of the Kamishiro fault in segments IVa and Va dips 30°–35° towards southeast, which would place these volcanic products on the hanging-wall of the fault (Fig. 7B). Geomorphological studies show no Quaternary fault displacement in segments VI and V where

the Kamishiro fault has no mapped surface trace (Togo et al., 1996; Kondo et al., 2008). It is plausible that Quaternary volcanism has covered the surface fault trace in the northern part of the Kamishiro fault and that the fault has not yet ruptured through these young units.

4.4. Modeling of the surface deformation

In order to check the validity of the proposed coseismic slip distribution inferred from the aftershock distribution, we calculated the surface deformation predicted from our proposed fault model and compared it to the InSAR data acquired by GSI. It should be noted that we do not intend to reproduce the exact surface displacement distribution in detail. Our goal is to simulate the large scale pattern observed in the interferogram, since aftershocks can mostly constrain the extent of the slip region. We assumed a simple homogeneous elastic half-space ignoring surface topography and made use of the analytical expressions for displacements due to fault slip by Okada (1992). In order to compensate for the weak sedimentary layers inside the NFM basin, rigidity was set at 20 GPa and the Poisson ratio was assumed to be 0.25. We use our proposed source fault configuration of a fault with a dip angle that steepens towards its deeper parts and check if this configuration can explain the observed surface deformation pattern (Case 1). For that we assumed that the largest coseismic slip region coincides with the seismic gaps observed in the shallow parts of the source fault inside segments IIa and IIIa and the deeper parts of the source fault inside IIIb and IVb. The centroid moment tensor solution estimated by JMA (Japan Meteorological Agency, 2014) coincides with our observations of a WNW-ESE reverse fault with a strike-slip component. Thus we assumed the same amount of slip for both the dip-slip and strike-slip components. We estimated an average slip of 1.37 m, by assuming uniform strike- and dip-slip distribution over the whole major slip region of our proposed source fault model in Table 3, to satisfy the seismic moment estimated by JMA (2.98×10^{18} Nm, Mw 6.24).

Consecutively, there are two hypotheses that need to be verified by our modeling with respect to where the largest coseismic slip occurred. First, we want to verify that the seismic gap areas are related to high coseismic slip whereas high concentration of aftershocks is related to small coseismic slip. To verify this hypothesis we tested the null hypothesis where, in addition to the areas described in Case (1), we examine the case that large coseismic slip also occurred in areas of high aftershock activity in segments IVa, IVa and Vb, and the southern edge of the fault in segments Ia and Ib (Case 2). Keeping the total seismic moment the same as the JMA moment, we assumed an average slip of 0.44 m, distributed uniformly over the whole region of our proposed source fault model (Table 3).

Second, we want to verify that there is currently no deformation related to the surface trace of the Otari–Nakayama fault. Thus, as the second null hypothesis, in addition to the areas described in Case (1), we assumed that coseismic slip occurred on the Otari–Nakayama fault at shallow depth (<4 km). We assumed a slip of 1.14 m over the whole major slip region of Case (1) and a slip of 0.57 m, half of the major slip, in the area marked by the blue rectangles above segments IIIb and IVb (Fig. 7A), keeping the total seismic moment same as that of the JMA estimated.

We compare the surface deformation pattern observed in the InSAR data to the calculated surface displacements of Cases 1, 2, and 3 (Fig. 8). The predicted line-of-sight (LOS) displacements show a two-lobed pattern where the hanging wall side moves towards the satellite and the footwall side moves away from the satellite (Fig. 8). We can see that the outermost fringe in the hanging wall in Fig. 8B shows better correlation with the slip region in Fig. 8A and D than that of Fig. 8C. In addition, calculated surface deformation in Cases (1) and (3) near the Kamishiro fault trace is large only in segments II and III (Fig. 8A, D), while in case (2) the model predicts large surface deformation from segment II through V (Fig. 8C). These observations make Case 2 the least likely hypothesis for where the majority of the coseismic slip occurred and

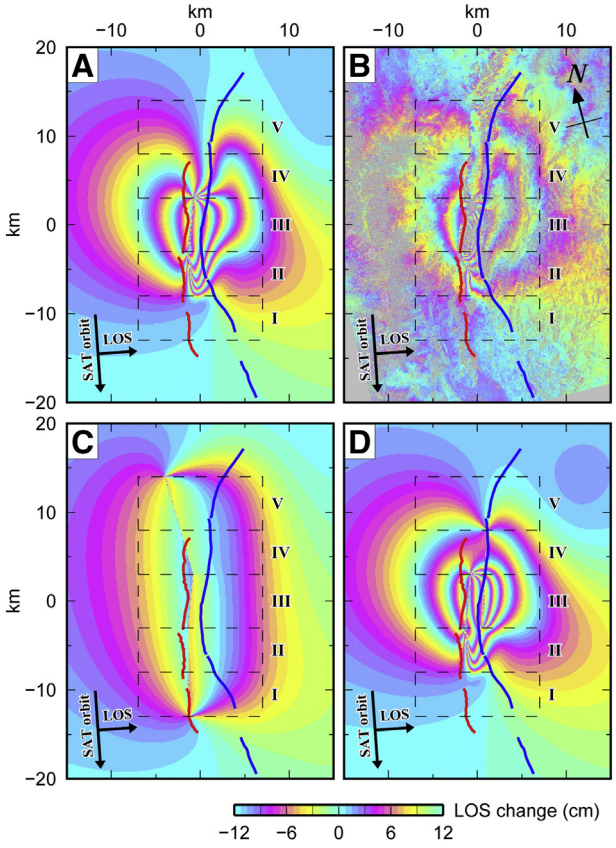

Fig 8. Calculation of surface deformation using the proposed source fault geometry. Red line: surface trace of the Kamishiro fault. Blue line: surface trace of the Otari–Nakayama fault. The absolute slip value is determined by assuming a uniform strike- and dip-slip distribution over the whole slip region to satisfy the seismic moment estimated by JMA (2.98×10^{18} Nm, Mw 6.24). A) Case 1, cyan polygons in Fig 7: Calculated Line of Sight (LOS) change values assuming major coseismic slip occurred only in the observed seismic gap areas, with an average slip of 1.37 m. B) Observed InSAR LOS change values analyzed by GSI from ALOS raw data of JAXA, METI (Geospatial Information Authority of Japan, 2014). C) Case 2, black and cyan polygons in Fig 7: Calculated LOS change values assuming major coseismic slip also occurred in the high seismic activity areas of segments IV and V, with an average slip of 0.44 m. D) Case 3, cyan and blue polygons in Fig 7: Calculated LOS change values assuming an average 1.14 m slip in the seismic gap areas and 0.57 in the shallow parts of the Otari–Nakayama fault (<4 km).

supports previous studies that suggest that areas with observed high concentration of aftershocks are related to small coseismic slip.

The interferogram displays a pattern of concentrated short wavelength deformation between the Kamishiro and Otari–Nakayama fault traces inside segment III and a long wavelength deformation to the east of the Otari–Nakayama fault trace spanning segments II to IV (Fig. 8B). Both in Cases 1 and 3, the large uplift and LOS displacements are concentrated near the upper edges of segments II and III (Fig. 8A,D), which is also consistent with the large surface displacements observed in the outcrop of the Kamishiro fault (Fig 8B). In Case 1, the outermost fringes of the two-lobed patterns are joined together at two points on the edges of segment III, which is consistent with the surveyed ends of the surface ruptures along Kamishiro fault (Geological Survey of Japan, AIST, 2014). Conversely in Case 3, the model predicts at the northern edge of segment IV an additional third point on the Otari–Nakayama fault trace where the outermost fringes of the two-lobed patters come together (Fig. 8D). This feature is not consistent with either the observed interferogram patterns (Fig. 8B) or with the geomorphological observations that showed that there was no surface rupture along the Otari–Nakayama fault trace (Geological Survey of Japan, AIST, 2014). In addition, if we assume that some coseismic slip occurred on the Otari–Nakayama at shallow depth (<4 km) as in case 3, then the model predicts more than 40 cm uplift in the area to the east

of the Otari–Nakayama surface fault trace in segments III and IV and 10–20 cm of subsidence in the area to the west of the Otari–Nakayama surface fault trace in segment IV. This feature is not observed in the interferogram (Fig. 8B), which makes it unlikely that significant amounts of slip occurred on the shallow parts of that fault. Considering these features, we conclude that Case 1 explains the observed interferogram better than Case 3. Thus we believe that the long-wavelength, small-magnitude surface deformation area to the east of the Otari–Nakayama fault trace accompanied by a larger amount of surface deformation along the Kamishiro fault trace, is the result of a source fault that dips with a higher angle at its deeper parts than the parts close to the surface as in our proposed source fault model.

4.5. Footwall shortcut

By combining aftershock distribution, InSAR data and Quaternary geomorphological evidence, we suggest that slip in both the present and Quaternary events, if any, reached the surface in segments II and III but not in segments IV and V. In addition, InSAR data shows no surface rupture associated with the Otari–Nakayama fault trace (Geospatial Information Authority of Japan, 2014) after the 2014 Northern Nagano earthquake (Figs. 7C, 8B). The Otari–Nakayama fault has been mapped in the field (e.g. Kato et al., 1989) although it is considered to have been inactive since the late Pleistocene (Matsuta et.al., 2004; Ueki, 2008). We may assume that the Otari–Nakayama fault represents an older high angle normal fault associated with the opening of the NFM rift basin that is reactivated by the Pliocene (3 Ma) tectonic inversion (e.g. Sato, 1994) (Fig. 9A). In that case we can explain the high dip-angle of the source fault at depths of 4–10 km under the NFM basin based on the aftershock distribution of the Northern Nagano earthquake. This high-angle fault is unfavorably oriented for thrust type faulting in the present day compressional regime. Thus its deeper part inside the basement rock is reactivated as an oblique fault, which is in accordance to the estimated focal mechanism solution of the main shock (Fig. 9B). In addition, this verifies the geodetic observations suggesting a maximum horizontal principal strain axis oblique to the strike of the ISTL (Sagiya et al., 2004).

The shallow part of the Otari–Nakayama fault that reaches the surface inside the weak sedimentary layers of the NFM basin should not be mechanically able to accommodate significant amounts of slip in the present day stress field. A lower angle fault is necessary in order to accommodate parts of the shortening deformation inside the basin. The lower angle of the source fault at 0–4 km depth indicates that Kamishiro fault developed as a footwall shortcut thrust which nucleated from the deeper part of Otari–Nakayama fault sometime after the middle to late Pleistocene (Fig. 9B). Although footwall shortcut faults have been documented in the geological literature (e.g. Powell, 1989; Butler et al., 2006; Pace et al., 2014), and their development has been modeled using analog experiments (e.g. McClay and Buchanan, 1992; Yamada and McClay, 2003; Amilibia et al., 2005), our study is the first to elucidate the deeper geometry of an active footwall shortcut using seismic data.

5. Conclusions

Precise relocation of the foreshock, main shock, and aftershock activity of the 2014 Northern Nagano earthquake provides us with new evidence about the geometry of the northernmost tip of the ISTL:

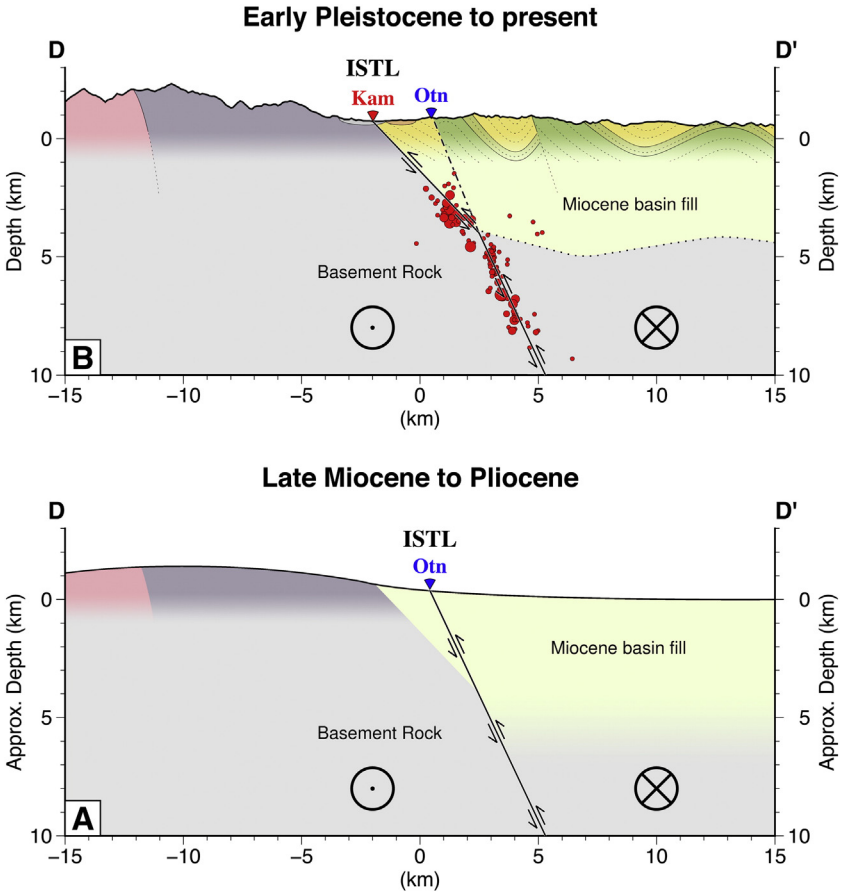

Fig. 9. Conceptual model of a footwall shortcut thrust in the Northern ISTL. Cross section location is shown in Fig. 7B. Red circles represent aftershock activity in segment II. Color convention for geological units is the same as in Fig. 2. The strata inclination is measured from the 1:50,000 geological map of the Omachi district (Kato et al., 1989). Bottom of basin is drawn at the Vp = 5.2 km/s contour from seismic tomography (Panayotopoulos et al., 2014).

1. The detailed aftershock distribution of the 2014 Northern Nagano Earthquake gives us the opportunity to map the source fault at depth. The upper part of the source fault dips 30°–45° SE and coincides with the surface trace of the Kamishiro fault, while the lower part of the source fault dips more steeply, at 50°–65° SE. We interpret the steeper segment to coincide with the deeper part of the Otari–Nakayama fault.
2. The focal mechanism solutions for aftershocks on the proposed source fault of the Northern Nagano earthquake exhibit both reverse and left-lateral components in accordance with the inherited fault geometry and the present-day stress field. Most aftershocks with a large strike-slip component are distributed along a branch fault with a steep dip-angle in the footwall side of the source fault.
3. It is suggested from the aftershock distribution that coseimic slip is greatest in the central part of the fault (Segments II–IV), at depths from 0 to 10 km, where we found a gap in aftershock distribution. This is supported by satellite data in which large surface deformation is found in the area of the aftershock gap. The northern parts of the fault are marked by increased aftershock activity and little surface deformation.
4. Movement on the shallower part of the source fault, where the dip angle is smaller, contributes to the short-wavelength, large-surface deformation near the Kamishiro fault. Movement on the deeper part of the source fault, where the dip angle is higher, contributes to the observed long-wavelength, small-magnitude surface deformation east of the surface trace of the Otari–Nakayama fault.
5. We conclude that, in areas where the surface traces of the Kamishiro and the Otari–Nakayama faults are visible, the Kamishiro fault developed as a low angle footwall shortcut thrust which nucleated from the deeper part of the high angle Otari–Nakayama fault in order to accommodate shortening deformation inside the NFM basin.

Acknowledgments

We wish to thank Shigeru Watanabe for assisting us with arrival time picking in the present study. We use waveform data from Hi-net, operated by the National Research Institute for Earth Science and Disaster Prevention (NIED), and from stations by Kyoto University. We use arrival time pickings from the Japan Meteorological Agency. The Geospatial Information Authority of Japan provided us with the InSAR image. We would also like to thank H. Zhang for the use of the TomoDD code. We appreciate Anne Van Horne for editing the manuscript. The images in this study were created using GMT, Generic Mapping Tools data processing software. The present study is supported by the Ministry of Education, Culture, Sports, Science and Technology (MEXT) of Japan, under its Earthquake and Volcano Hazards Observation and Research Program, the Special Project for Reducing Vulnerability for Urban Mega-earthquake Disasters, and JSPS KAKENHI Grant-in-Aid for Scientific Research (S) Grant Number 25220202.

References

Amilibia, A., McClay, K.R., Sabat, F., Munoz, J.A., Roca, E., 2005. Analogue modelling of inverted oblique rift systems. Geol. Acta 3 (3), 251–271. http://dx.doi.org/10.1344/105.000001395.

Asano, Y., Saito, T., Ito, Y., Shiomi, K., Hirose, H., Matsumoto, T., Aoi, S., Hori, S., Sekiguchi, S., 2011. Spatial distribution and focal mechanisms of aftershocks of the 2011 off the Pacific coast of Tohoku earthquake. Earth Planets Space 63, 669–673. http://dx.doi.org/10.5047/eps.2011.06.016.

Beroza, G.C., Zoback, M.D., 1993. Mechanism diversity of Loma Prieta aftershocks and the mechanics of mainshock-aftershock interaction. Science 259, 210–213. http://dx.doi.org/10.1126/science.259.5092.210.

Boyer, S.E., Elliott, D., 1982. Thrust systems. Bull. Am. Assoc. Pet. Geol. 66 (9), 1196–1230.

Butler, R.W.H., Tavarnelli, E., Grasso, M., 2006. Structural inheritance in mountain belts: an alpine–apennine perspective. J. Struct. Geol. 28, 1893–1908. http://dx.doi.org/10.1016/j.jsg.2006.09.006.

Editorial committee of civil engineering geologic map of Kanto, 1996n. Civil Engineering Geologic Map of Kanto 1:200,000. Japan Institute of Construction Engineering, p. 768 (in Japanese).

Felzer, K.R., Brodsky, E.E., 2006. Decay of aftershock density with distance indicates triggering by dynamic stress. Nature 441 (7094), 735–738. http://dx.doi.org/10.1038/nature04799.

Geological Survey of Japan, AIST, 2014. Surface rupture and deformation associated with the Nagano-ken Hokubu earthquake in 2014. Report of the Coordination Committee for Earthquake Prediction. 93, pp. 265–276 (in Japanese, available online: http://cais.gsi.go.jp/YOCHIREN/report/kaihou93/07_01.pdf).

Geological Survey of Japan, 2003. Geological map of Japan 1:1,000,000, 3rd edition, 2nd CD-ROM version. Digital Geoscience Map G-1. Japan, Geological Survey of.

Geospatial Information Authority of Japan, 2014. Crustal deformation associated to the Northern Nagano earthquake observed by the "Daichi-2" ALOS-2 satellite. in Japanese, available online http://www.gsi.go.jp/BOUSAI/h26-nagano-earthquake-index.html.

Hardebeck, J.L., Shearer, P.M., 2002. A new method for determining first-motion focal mechanisms. Bull. Seismol. Soc. Am. 92, 2264–2276. http://dx.doi.org/10.1785/0120010200.

Hardebeck, J.L., Shearer, P.M., 2003. Using S/P amplitude ratios to constrain the focal mechanisms of small earthquakes. Bull. Seismol. Soc. Am. 93, 2434–2444. http://dx.doi.org/10.1785/0120020236.

Hirata, N., Matsu'ura, M., 1987. Maximum-likelihood estimation of hypocenters with origin time eliminated using nonlinear inversion technique. Phys. Earth Planet. Inter. 47, 50–61. http://dx.doi.org/10.1016/0031-9201(87)90066-5.

Hirata, N., Ohmi, S., Sakai, S., Katsumata, K., Matsumoto, S., Takanami, T., Yamamoto, A., Iidaka, T., Urabe, T., Sekine, M., Ooida, T., Yamazaki, F., Katao, H., Umeda, Y., Nakamura, M., Seto, N., Matsushima, T., Shimizu, H., 1996. Japanese university group of the urgent joint observation for the 1995 Hyogo-ken Nanbu earthquake. Urgent Joint Observation of Aftershocks of the 1995 Hyogo-ken Nanbu Earthquake. Journal of Physics of the Earth 44, pp. 317–328.

Ikeda, Y., 1983. Thrust Front Migration and its Mechanism: Evolution of Intraplate Thrust Systems. Bulletin of the Department of Geography 15. the University of Tokyo, pp. 125–159.

Imanishi, K., Kuwahara, Y., Cho, I., Panayotopoulos, Y., Hirata, N., 2010. Present-day stress field along the Itoigawa–Shizuoka tectonic line active fault system by microearthquake observation. Abstract SSS017-07 Presented at Japan Geoscience Union Meeting 2010, Chiba-city, Japan, 23–28 May.

Japan Meteorological Agency, 2014. Monthly report on earthquakes and volcanoes in Japan, November 2014. in Japanese, available online http://www.data.jma.go.jp/svd/eqev/data/gaikyo/monthly/201411/201411monthly.pdf.

Kano, K., Kosaka, K., Murata, A., Yanai, S., 1990. Intra-arc deformations with vertical rotation axes: the case of the pre-Middle Miocene terranes of Southwest Japan. Tectonophysics 176, 333–354. http://dx.doi.org/10.1016/0040-1951(90)90077-L.

Kato, A., Miyatake, T., Hirata, N., 2010. Asperity and barriers of the 2004 Mid-Niigata prefecture earthquake revealed by highly dense seismic observations. Bull. Seismol. Soc. Am. 100 (1), 298–306. http://dx.doi.org/10.1785/0120090218.

Kato, H., Mimura, K., Sato, T., Takizawa, F., 1989. Geology of the Omachi District Quadrangle Series, scale 1:50,000. Geol. Surv. Jpn (available online from: https://www.gsj.jp/Map/JP/geology4.html).

Kato, H., 1992. Fossa Magna—a masked border region separating southwest and northeast Japan. Bull. Geol. Surv. Jpn 43, 1–30.

Kondo, H., Toda, S., Okumura, K., Takada, K., 2006. Geomorphic features indicating strike-slip movement along the East Matsumoto Basin Faults, Itoigawa–Shizuoka Tectonic Line active fault system, Central Japan. J. Geogr. 115 (2), 208–220 (in Japanese with English abstract).

Kondo, H., Toda, S., Okumura, K., Takada, K., Chiba, T., 2008. A fault scarp in an urban area identified by LiDAR survey: a case study on the Itoigawa–Shizuoka Tectonic Line, central Japan. Geomorphology 101, 731–739. http://dx.doi.org/10.1016/j.geomorph.2008.02.012.

Matsuta, N., Ikeda, Y., Sato, H., 2004. The slip-rate along the northern Itoigawa–Shizuoka tectonic line active fault system, central Japan. Earth Planets Space 56, 1323–1330.

McClay, K.R., Buchanan, P.G., 1992. Thrust faults in inverted extensional basins. In: McClay, K.R. (Ed.), Thrust Tectonics, pp. 93–104.

Mendoza, C., Hartzell, S.H., 1988. Aftershock patterns and main shock faulting. Bull. Seismol. Soc. Am. 78 (4), 1438–1449.

Nakano, S., Takeuchi, M., Yoshikawa, T., Nagamori, H., Kariya, Y., Okumura, K., Taguchi, Y., 2002. Geology of the Shiroumadake District Quadrangle Series, scale 1:50,000. Geological Survey of Japan. (available online from: https://www.gsj.jp/Map/JP/geology4.html)

Nakata, T., Imaizumi, T. (Eds.), 2002. Digital Active Fault Map of Japan. University of Tokyo Press, Tokyo.

National Research Institute for Earth Science and Disaster Prevention, 2014r. NIED seismic moment tensor catalogue. National Research Institute for Earth Science and Disaster Prevention. (available online from: http://www.fnet.bosai.go.jp/event/joho.php?LANG=en).

Okada, Y., 1992. Internal deformation due to shear and tensile faults in half-space. Bull. Seismol. Soc. Am. 82, 2,1014–2,1040.

Okumura, K., Imura, R., Imaizumi, T., Togo, M., Sawa, H., Mizuno, K., Kariya, Y., 1998. Recent surface faulting events along the northern part of the Itoigawa–Shizuoka Tectonic Line: trenching survey of the Kamishiro Fault and East Matsumoto Basin Faults, central Japan. J. Seismol. Soc. Jpn (Zisin) 50, 35–51 (in Japanese with English abstract).

Okumura, K., 2001. Paleoseismology of the Itoigawa–Shizuoka tectonic line in central Japan. J. Seismol. 5, 411–431. http://dx.doi.org/10.1023/A:1011483811145.

Oppenheimer, D.H., Bakun, W.H., Lindh, A.G., 1990. Slip partitioning of the Calaveras Fault, California, and prospects for future earthquakes. J. Geophys. Res. 95 (B6), 8483–8498. http://dx.doi.org/10.1029/JB095iB06p08483.

Otofuji, Y., Matsuda, T., Noda, S., 1985. Paleomagnetic evidence for Miocene counter-clockwise rotation of Northeast Japan — rifting process of the Japan arc. Earth Planet. Sci. Lett. 75, 265–277. http://dx.doi.org/10.1016/0012-821X(85)90108-6.

Pace, P., Domenica, A.D., Calamita, F., 2014. Summit low-angle faults in the Central Apennines of Italy: younger-on-older thrusts or rotated normal faults? Constraints for defining the tectonic style of thrust belts. Tectonics 33, 756–785. http://dx.doi.org/10.1002/2013TC003385.

Panayotopoulos, Y., Hirata, N., Sato Kato, A., Imanishi, K., Kuwahara, Y., Cho, I., Takeda, T., Asano, Y., 2014. Investigating the role of the Itoigawa–Shizuoka tectonic line towards the evolution of the Northern Fossa Magna rift basin. Tectonophysics 615, 12–26. http://dx.doi.org/10.1016/j.tecto.2013.12.014.

Powell, C.M., 1987. Inversion tectonics in S.W. Dyfed. Proc. Geol. Assoc. 98 (3), 193–203. http://dx.doi.org/10.1016/S0016–7878(87)80037–8.

Powell, C.M., 1989. Structural controls on Palaeozoic basin evolution and inversion in southwest Wales. J. Geol. Soc. Lond. 146 (1989), 439–446. http://dx.doi.org/10.1144/gsjgs.146.3.0439.

Sagiya, T., Nishimura, T., Iio, Y., Tada, T., 2002. Crustal deformation around the northern and central Itoigawa–Shizuoka Tectonic Line. Earth Planets Space 54, 1059–1063.

Sagiya, T., Nishimura, T., Iio, Y., 2004. Heterogeneous crustal deformation along the central-northern Itoigawa–Shizuoka Tectonic Line Fault system, Central Japan. Earth Planets Space 56, 1247–1252.

Sakai, S., 2004. Seismicity of the northern part of the Itoigawa–-Shizuoka Tectonic Line. Earth Planets Space 56, 1279–1283.

Sato, H., 1994. The relation between late Cenozoic tectonic events and stress field and basin development in northeast Japan. J. Geophys. Res. 99, 22261–22274. http://dx.doi.org/10.1029/94JB00854.

Sato, H., 1996. Inversion tectonics of Japanese Islands. Active Fault Research (Katsudansokenkyu) 15, 128–132 (in Japanese).

Sato, H., Hirata, N., 1998. Deep structure of active faults and evolution of the Japanese islands. Sci. J. (Kagaku) 68, 63–71 (in Japanese).

Sato, H., Iwasaki, T., Kawasaki, S., Ikeda, Y., Matsuta, N., Takeda, T., Hirata, N., Kawanaka, T., 2004. Formation and shortening deformation of a back-arc rift basin revealed by deep seismic profiling, central Japan. Tectonophysics 388, 47–58. http://dx.doi.org/10.1016/j.tecto.2004.07.004.

Shinohara, M., Machida, Y., Yamada, T., Nakahigashi, K., Shinbo, T., Mochizuki, K., Murai, Y., Hino, R., Ito, Y., Sato, T., Shiobara, H., Uehira, K., Yakiwara, H., Obana, K., Takahashi, N., Kodaira, S., Hirata, K., Tsushima, H., Iwasaki, T., 2012. Precise aftershock distribution of the 2011 off the Pacific coast of Tohoku earthquake revealed by an ocean-bottom seismometer network. Earth Planets Space 64, 1137–1148. http://dx.doi.org/10.5047/eps.2012.09.003.

Taira, A., 2001. Tectonic evolution of the Japanese island arc system. Annu. Rev. Earth Planet. Sci. 29, 109–134. http://dx.doi.org/10.1146/annurev.earth.29.1.109.

Takano, O., 2002. Changes in depositional systems and sequences in response to basin evolution in a rifted and inverted basin: an example from the Neogene Niigata–Shin'etsu basin, Northern Fossa Magna, central Japan. Sediment. Geol. 152 (1–2), 79–97. http://dx.doi.org/10.1016/S0037-0738(01)00286-X.

Takeda, T., Sato, H., Iwasaki, T., Matsuta, N., Sakai, S., Iidaka, T., Kato, A., 2004. Crustal structure in the northern Fossa Magna region, central Japan, modeled from refraction/wide-angle reflection data. Earth Planets Space 56, 1293–1299.

Togo, M., Ikeda, Y., Imaizumi, T., Sato, H., 1996. Fault morphology of both ends of the Kamishiro fault along the Itoigawa–-Shizuoka Tectonic Line, central Japan. Active Fault Res. (Katsudansokenkyu) 15, 9–16 (in Japanese with English Abstract).

Ueki, T., 2008. Plio-Pleistocene behavior of the Itoigawa–Shizuoka Tectonic Line in Northern Nagano Prefecture, Central Japan: paleomagnetism of the Omine-SK Tephra. Bulletin of the Earthquake Research Institute, the University of Tokyo 83, 163–173 (in Japanese with English abstract).

Waldhauser, F., Ellsworth, W.L., 2000. A double-difference earthquake location algorithm: method and application to the northern Hayward fault, California. Bull. Seismol. Soc. Am. 90 (6), 1353–1368. http://dx.doi.org/10.1785/0120000006.

Williams, G.D., Powell, C.M., Cooper, M.A., 1989. Geometry and kinematics of inversion tectonics. In: Cooper, M.A., Williams, G.D. (Eds.), Inversion Tectonics. Geological Society of London Special Publication 44, pp. 3–15.

Woessner, J., Schorlemmer, D., Wiemer, S., Mai, P.M., 2006. Spatial correlation of aftershock locations and on-fault main shock properties. J. Geophys. Res. 111, B08301. http://dx.doi.org/10.1029/2005JB003961.

Yabe, H., 1918. Itoigawa–Shizuoka Tectonic Line. Modern Scirnce (Gendainokagaku) 6, 147–150 (in Japanese).

Yamada, Y., McClay, K., 2003. Application of geometric models to inverted listric fault systems in sandbox experiments. Paper 2: insights for possible along strike migration of material during 3D hanging wall deformation. J. Struct. Geol. 25, 1331–1336. http://dx.doi.org/10.1016/S0191-8141(02)00160-8.

Yamaji, A., 1990. Rapid intra-arc rifting in Miocene Northeast Japan. Tectonics 9, No. 3, 365–378. http://dx.doi.org/10.1029/TC009i003p00365.

Zhang, H., Thurber, C.H., 2003. Double-difference tomography: the method and its application to the Hayward Fault, California. Bull. Seismol. Soc. Am. 93 (5), 1875–1889. http://dx.doi.org/10.1785/0120020190.